



Low Temperature Plasma Technology Laboratory

Design of a permanent-magnet helicon reactor

Francis F. Chen and Humberto Torreblanca

LTP-601

January, 2006

NSF Final Report not intended for publication



Electrical Engineering Department
Los Angeles, California 90095-1594

Design of a permanent-magnet helicon reactor

Francis F. Chen and Humberto Torreblanca

Electrical Engineering Department, University of California, Los Angeles 90095-1594

ABSTRACT

A helicon source consisting of multiple discharge tubes, capable of covering arbitrarily large areas with uniform density of at least 10^{12} cm^{-3} , is described. The dc magnetic field is provided by permanent magnets. The design of the tube dimensions and shape, of the magnet structure and placement, and of the radiofrequency (rf) system, including frequency, matching circuit, and antenna, was optimized by numerical calculations supplemented by experimental measurements on single tubes. This reactor concept can be applied to processing of semiconductors, flat-panel and flexible displays, web-coating of plastic films, and optical coatings.

I. INTRODUCTION

That large-area uniform plasmas can be produced with an array of individual helicon sources has previously been shown by Chen et al.¹ Helicon discharges can create high plasma densities with relatively small rf power because of a unique absorption mechanism based on the launching of waves in the plasma. These waves require a dc magnetic field (B-field). In the previous work, the B-field was provided by a large electromagnet surrounding the entire array. This arrangement is obviously inappropriate for large arrays covering substrates of meter dimensions. We have devised a permanent magnet configuration which can be applied to each of an arbitrary number of discharge tubes without recursive field lines which prevent ejection of plasma toward a distant substrate. This method avoids the cost and weight of a large electromagnet and its power supply.

The results are shown first in this section. The design considerations constitute the balance of this paper. Figure 1 shows a discharge tube consisting of a ceramic, quartz, or pyrex vessel capped at the top by a conducting flange with a gas-feed inlet, and exposed to the processing chamber at the bottom end. An $m = 0$ loop antenna of several turns is shown.

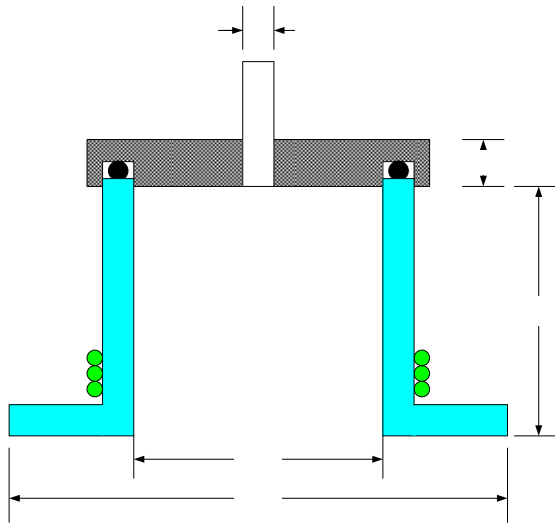


Fig 1. Design of the discharge tube.

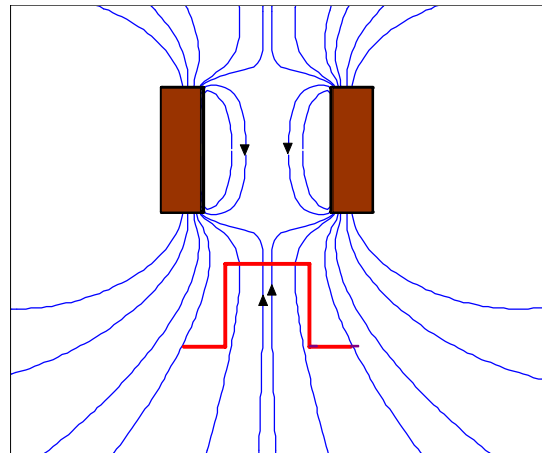


Fig. 2. Magnetic field lines from a stack of annular magnets (brown rectangles). The discharge tube is shown in red in its designed position.

Figure 2 shows the field lines from a permanent magnet stack and the position of the discharge tube in relation to them. Note that the tube is not in the strong field region inside the magnet rings because the field lines there do not extend beyond the stagnation point near the bottom of the magnets. The tube is placed in the more uniform region in the far-field of the magnets.

Figure 3 shows a linear array of tubes to produce a wide strip of plasma, as would be used in a web-coater. Each individual source consists of a stack of ring magnets of 3" ID and 5" OD. The central circles depict the 2" diameter of the plasma inside the tubes. The encircling rectangle represents a soft iron plate used to mount the magnets. This is shown in detail in Fig. 5. Figure 4 shows a circular array of tubes such as used in Ref. 1. To cover larger circular substrates, additional circles of tubes can be added.

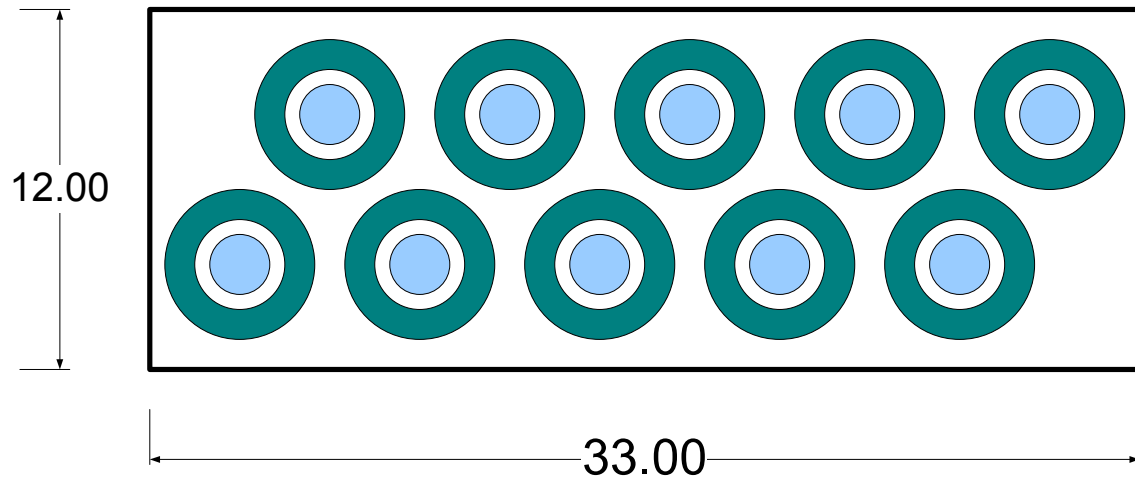


Fig 3. A linear array of helicon sources, each with its own magnets.

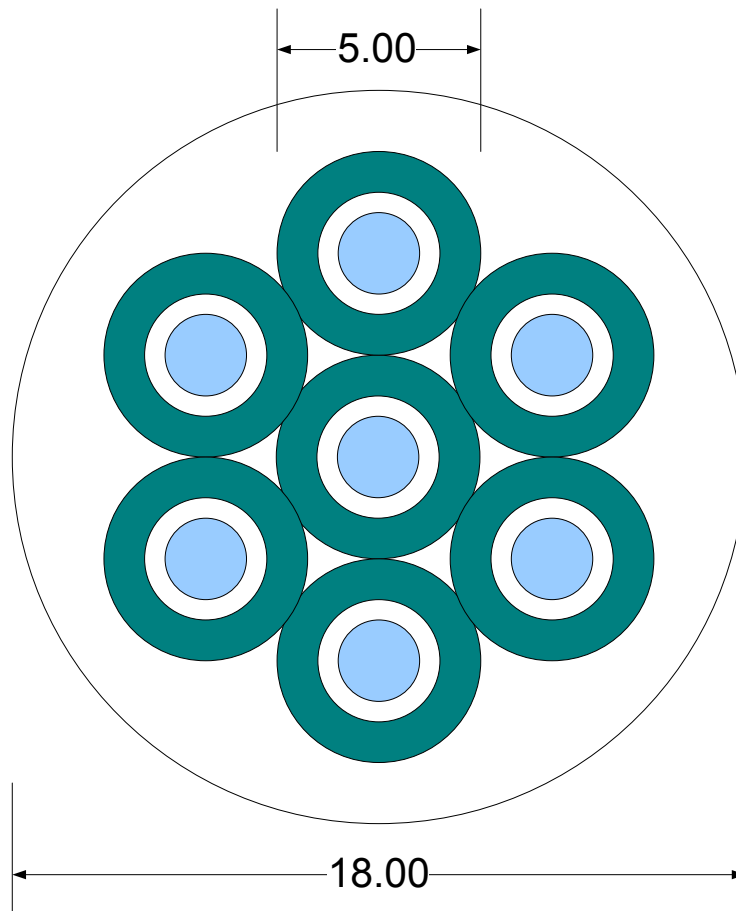


Fig. 4. A circular array of helicon sources.

Figure 5 shows mounting of adjacent tubes. The discharge tubes are sealed with O-rings over holes in the top cover of the vacuum chamber. Each tube has a “skirt” which isolates the

antenna from the conducting top plate, thus reducing the image currents induced on the latter. As the plasma flows from source into the chamber, the edges of the exit aperture will charge negatively to the floating potential. This has the effect of bending the ion orbits outward, thus spreading the plasma faster than by diffusion alone. The magnets are positioned by indentations in a soft iron cover, from which the magnets are suspended magnetically. The iron serves as a return path for the magnetic flux. The iron plate rests on aluminum or stainless steel posts resting on the top flange. The strength of the magnetic field in the discharge can be varied by changing the length of the support posts or the number of magnet rings in each stack.

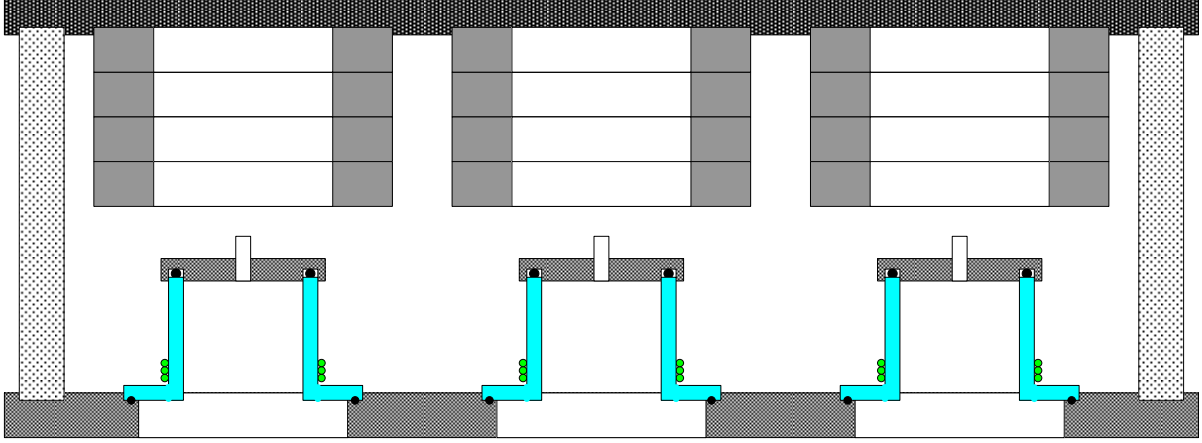


Fig. 5. Mounting of discharge tubes and magnets in an array of sources.

II. POWER BALANCE

Optimization of the discharge parameters—namely, the diameter and length of the tube and the strength of the magnetic field (B-field)—relies on calculations of the characteristics of the helicon wave done with the HELIC code.² This code yields the loading resistance R_p of the plasma, which is used to compute the rf power actually delivered to the plasma, P_{in} , from the antenna for a given power output P_{rf} from the rf generator. The losses in the matching circuit, antenna, and cables are represented by a circuit resistance R_c . The plasma power is given by the voltage division relation

$$P_{in} = P_{rf} \frac{R_p}{R_p + R_c}. \quad (1)$$

In Fig. 6, the orange curve shows R_p vs. density n as calculated by HELIC for three values of B . These curves show the low-field peak³ of helicons, which will be discussed later. The flatter curves show the corresponding curves for P_{in}/P_{rf} for three values of R_c . In all cases for $R_c = 0.1 \Omega$, it is seen that P_{in}/P_{rf} is essentially constant for R_p greater than about 1Ω , or $10R_c$. For $R_c > 0.1 \Omega$, the efficiency increasingly varies with n . At 40G, R_p never reaches 1Ω , and the efficiency is always peaked. The object is to design discharges with large R_p so that the transfer efficiency is $> 90\%$ over a large range of n for reasonable values of R_c . Note that the peak of R_p increases with increasing B . This is a consequence of the basic helicon dispersion relation

$$k_{tot} = \frac{\omega}{k_z} \frac{ne\mu_0}{B}, \quad k_{tot}^2 = k_{\perp}^2 / k_z^2, \quad (2)$$

which shows that n is proportional to B if all else is constant.

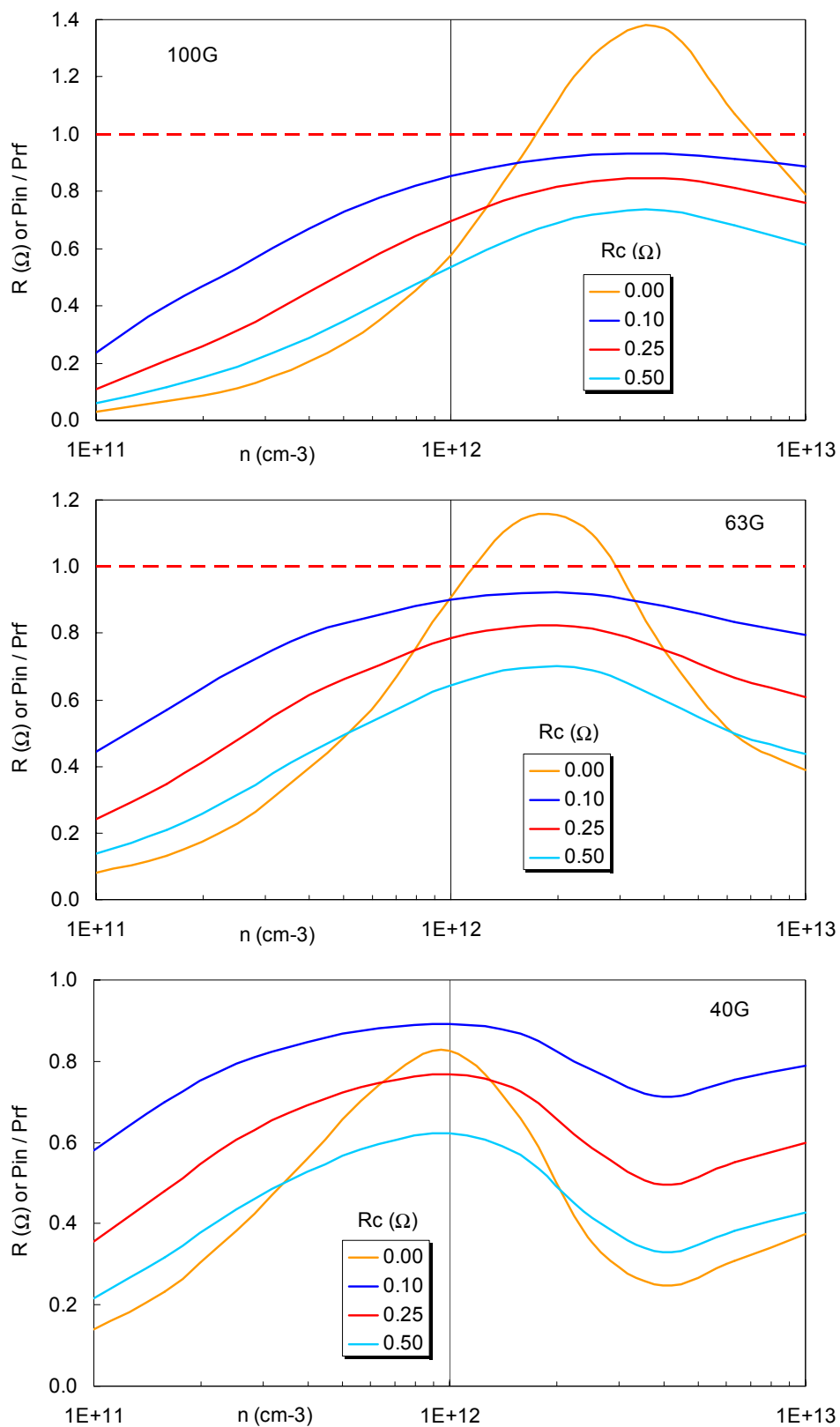


Fig. 6. Plasma resistance R vs density n at $B = 100, 63,$ and 40 G (orange curves). The lower curves are the transfer efficiency P_{in}/P_{rf} for three values of circuit resistance R_c .

The operating density depends on a balance between power in and power lost. Shamrai⁴ showed that the P_{out} curve will be proportional to n ; and if the P_{in} vs. n curve is not monotonic, a stable operating point is possible if the P_{in} and P_{out} curves cross where the P_{in} curve has a negative slope. An example is shown in Fig. 7. Here there is only one intersection, and it is a stable point because if n falls, P_{in} increases, thus increasing n back to the stable point, and *vice versa*.

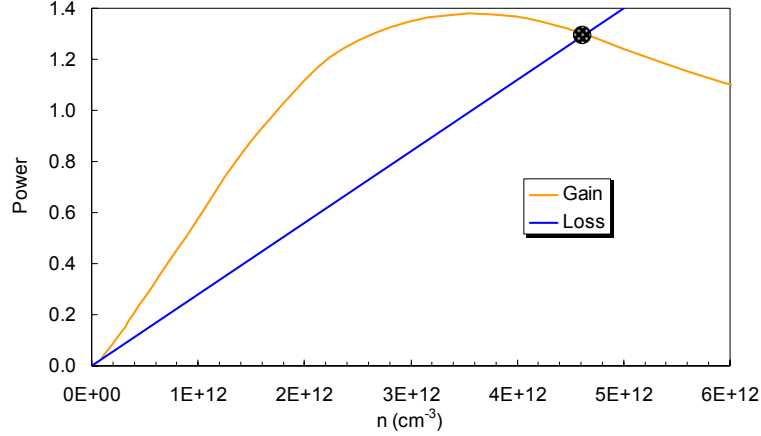


Fig. 7. Example of a stable intersection of the power-in and power-out curves, thus defining the operating point of the discharge.

To calculate the density expected at each P_{rf} , we need to consider the energy losses. The B-field of helicon discharges is too weak to confine ions. Electrons will be confined in the direction perpendicular to \mathbf{B} , but their losses through the sheaths at the ends of short tubes will dominate. The end result is that the electrons are not well confined, and the plasma losses are determined only by the ion losses, the electrons following at the same rate in order to preserve quasi-neutrality. At low pressure, the ions free-fall to the sheaths at the walls, and their loss rate is given by the density n_s at the sheath edge and the Bohm velocity c_s :

$$\Gamma_i = n_s c_s \approx \frac{1}{2} n_0 c_s. \quad (3)$$

The surface area of a tube 2" in diam and 2" long is $S = 122 \text{ cm}^2$, and the acoustic velocity at 3eV is

$$c_s = (KT_e / M)^{1/2} = 1.7 \times 10^5 \text{ cm/sec}. \quad (4)$$

The total loss rate is then

$$-dN / dt = \frac{1}{2} S n c_s = 1.0 \times 10^7 n \text{ sec}^{-1}. \quad (5)$$

In steady state, each ion-electron pair that is lost carries away an energy^{5,6}

$$W = E_c + W_i + W_e, \quad (6)$$

where $E_c(T_e)$ is the Vahedi⁷ curve, which gives the energy required to ionize each argon atom, including the energy lost in inelastic collisions. Each ion lost to the walls loses its energy gained in the presheath ($\frac{1}{2}KT_e$) and that gained in the wall sheath ($\approx 5KT_e$), a total of $W_i \approx 5.5KT_e$. The accompanying electron loses $2KT_e$.^{5,6} Since $E_c(3\text{eV}) \approx 43\text{eV}$, we have in this case $W \approx 50.5\text{eV}$. From Eq. (5), the total power lost, which must be replenished by P_{in} , is then

$$P_{out} \approx (50.5)(10^7)ne = 1.1 \times 10^{-10} n \text{ watts} \quad (7)$$

At high pressure, the ion loss rate will be decreased by ion-neutral collisions. For $T_e \gg T_i$, the flux is given by

$$\Gamma = -D_a \nabla n, \quad D_a \approx (KT_i / e) \mu_i (1 + T_e / T_i) \approx (KT_e / e) \mu_i, \quad (8)$$

where μ_i is the Ar^+ mobility in neutral argon and is proportional to the pressure p_0 . As a rough approximation, we may take $|\nabla n / n| \approx 1/2a$, a being the discharge radius. The outward flux is then the minimum of Eqs. (3) and (8), as shown in Fig. 8. We see that the collisionless approximation is valid up to about 9 mTorr and has the value $1.1 \times 10^{-10} n$ Watts.

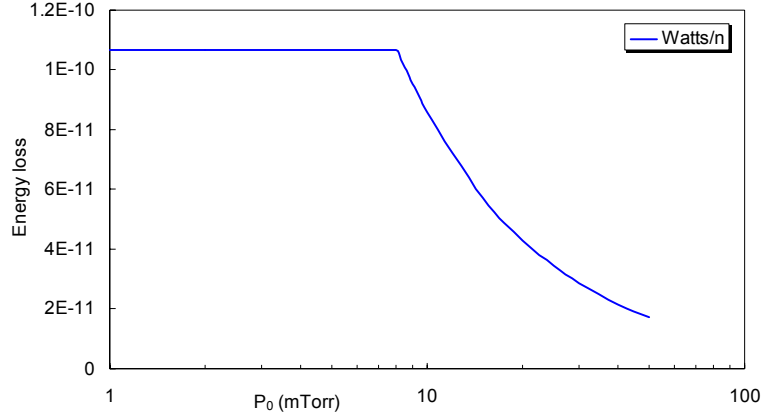


Fig. 8. Energy loss rate per unit density vs. pressure.

Using this value, we can draw plots of the type of Fig. 7, using the computed curves of Fig. 6, to get an idea of the density achievable with various rf powers. For instance, the 100-G case is shown in Fig. 9. This shows with $P_{\text{rf}} = 500\text{W}$ the peak density will be $\approx 5 \times 10^{12} \text{ cm}^{-3}$.

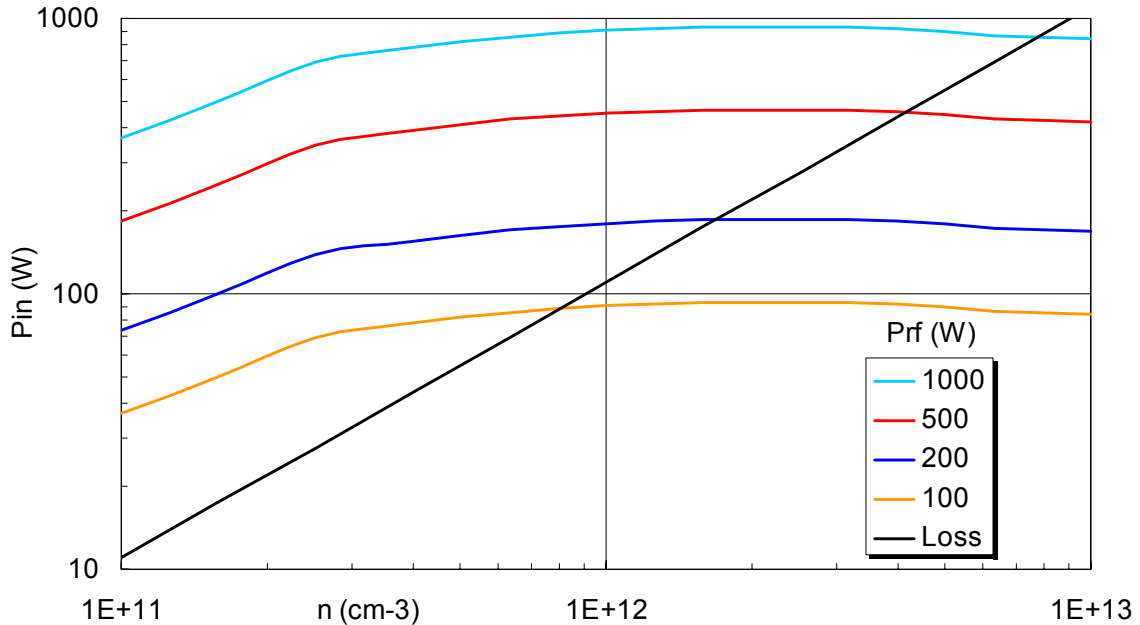


Fig. 9. Power in and out of the discharge vs. n at various P_{rf} , showing the density achievable with $R_c = 0.1\Omega$.

III. DESIGN OF THE DISCHARGE TUBE

A. The low-field peak

Although the basic helicon dispersion relation of Eq. (2) predicts n increasing linearly with B , a peak in n was found to occur at low B-fields. This has been explained by constructive interference from the wave reflected from the endplate.^{3,8} The peak in R_p causing the density peak will be prominent in the computations presented here, since operation with permanent magnets concerns low B-fields in the relevant range.

B. HELIC survey of parameters

The HELIC program² calculates wave propagation and absorption with different antennas and tube radii and lengths. Though the radial density, pressure, and electron temperature profiles are arbitrary, the n and B profiles in the axial (z) direction must be uniform. The results, therefore, are only a rough guide to the design. The geometry assumed in the program is shown in Fig. 10. The plasma and antenna radii are a and b , respectively. In addition, there is a ground plane at a large radius of 20 or 30 cm. To simulate injection into a large chamber, the tube length is assigned a large value of 200 cm. The actual tube length is adjusted with the distance H between the midplane of the antenna and the nearer endplate. The endplate can be an insulator or a conductor. In most of this work a simple loop antenna is used.

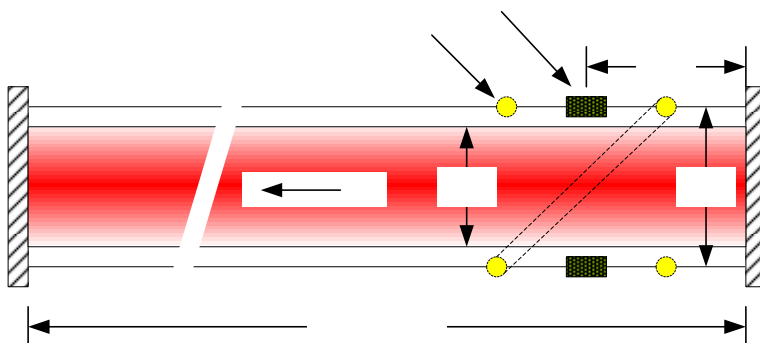


Fig. 10. Geometry of HELIC calculations.

1. Variation with magnetic field.

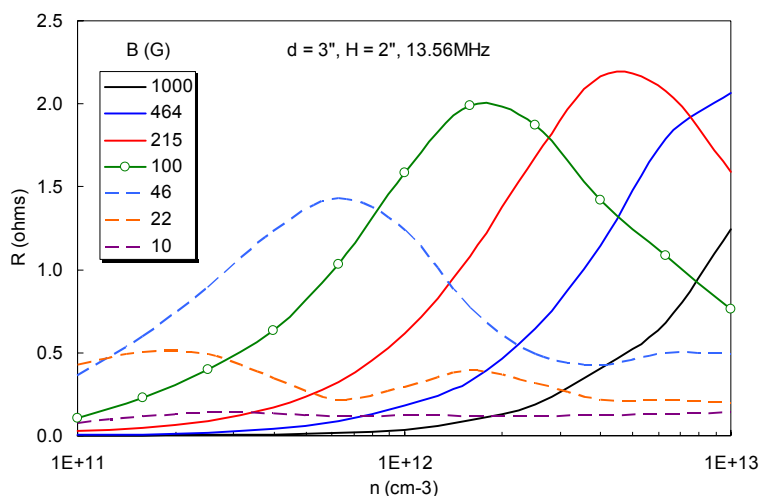


Fig. 11. Example of R_p - n curves showing the low-field peak. The points mark a target field of 100G.

Helical anten

Figure 11 shows that the peak in loading moves to higher n as B increases. To get 10^{12} cm^{-3} at the substrate would require densities in the upper 10^{12} cm^{-3} range inside the tube. We see that this requires $B \approx 100\text{-}400\text{G}$. The dashed curves are for fields that are too low for this tube size and frequency, and the 1000G curve peaks at too high a density.

2. Variation with tube diameter

Figure 12 shows R_p - n curves as the tube diameter d is varied. The loading increases

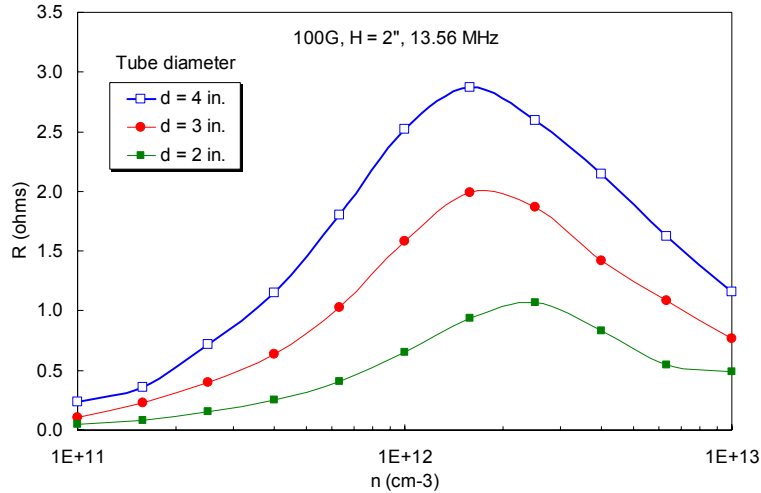


Fig. 12 Example of R_p - n curves as the tube diameter is varied.

greatly with wider tubes, but this benefit is not useful. As shown above, the rf transfer efficiency is close to 90% for $R_p > 1\Omega$. Furthermore, it takes much higher P_{rf} to fill a large tube, and the matching circuit is harder to design because of the inductance of the larger antenna.

3. Variation with tube length

The position and amplitude of the low-field peak depend on tube length L , which affects the range of the antenna position H ; but they also depend on n , B , and a , since these control the wavelength, according to Eq. (2). One example is shown in Fig. 13. In this case,

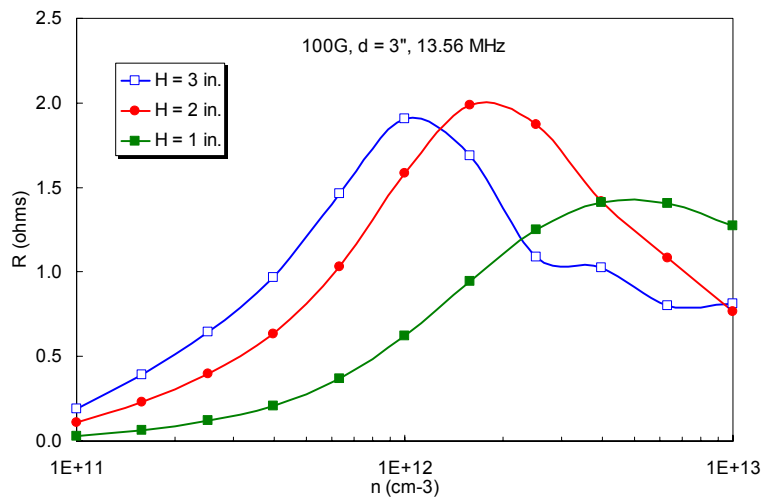


Fig. 13. Example of the variation with the distance H between the antenna and the endplate.

$H = 2\text{-}3''$ seems to be optimal, while $H = 1''$ is a little too low. These examples were calculated assuming a uniform plasma. In the final design, the radial n profile will be taken into account, and the results will be somewhat different.

4. Variation with frequency

The frequencies readily available in commercial rf power supplies are few in number, and these have a large effect on the size of individual tubes. In Fig. 14, we see that for small

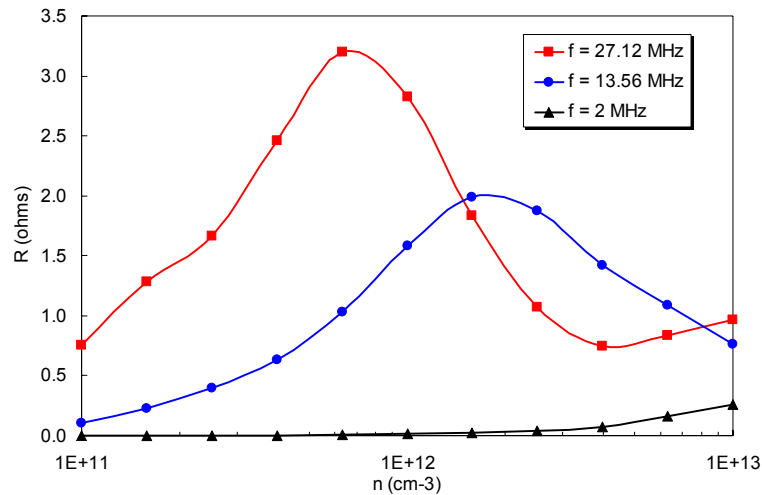


Fig. 14. Example of loading curves at three frequencies for $d = 3''$, $H = 2''$, $B = 100\text{G}$, and $p = 3\text{mTorr}$.

tubes of the type we are considering the normal frequency of 13.56 MHz is almost ideal. At the harmonic at 27.12 MHz, R_p is indeed higher, but we saw in Sec. II that coupling efficiency is already high for $R_p > 1\Omega$, and that happens for higher n at 13.56 MHz. At 2 MHz, the loading is an order of magnitude smaller, as seen more clearly at various B-fields in Fig. 15 comparing 2 with 13 MHz. The reason for this is not obvious. If we look at the wave fields at these two frequencies (Fig. 16), we see that $|\mathbf{B}|$ at $r = 0$ is larger in the source at 2 MHz. However, the power deposition (Fig. 17) is larger at 13 MHz. The reason is that the

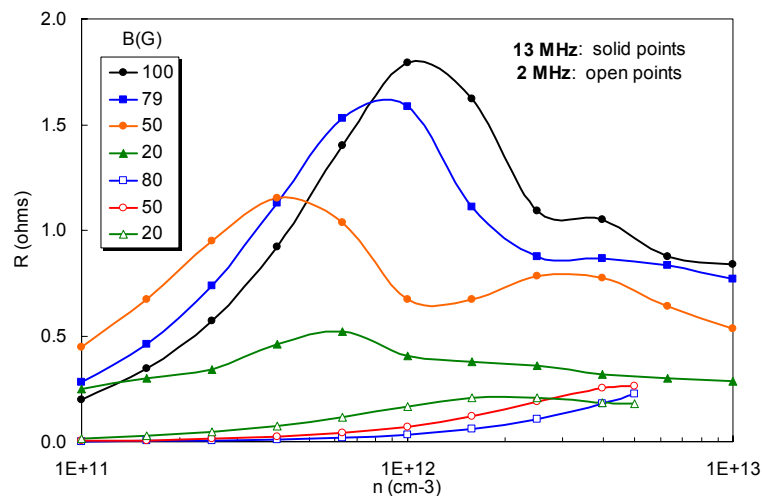


Fig. 15. Loading curves of a 3'' diam tube at two frequencies at various B-fields for $KT_e = 2\text{eV}$ and 10 mTorr.

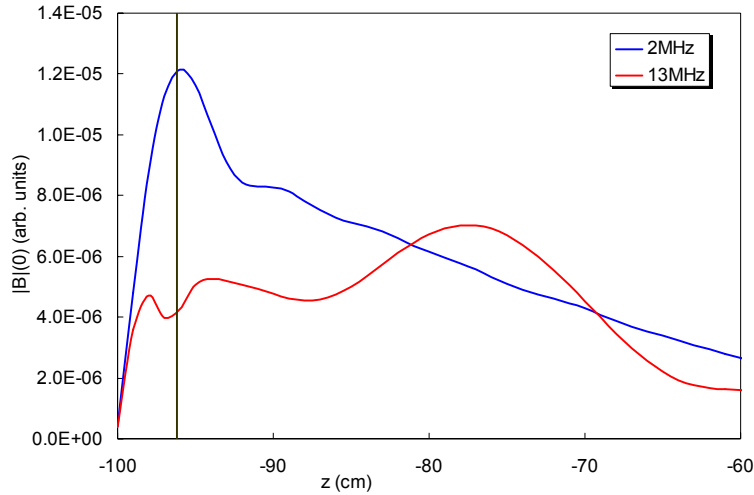


Fig. 16. Magnitude of wave B-field on axis vs z at 2 and 13.56 MHz. A conducting endplate is at the left, and the antenna is at the vertical line. Conditions are 3" diam, $H = 1.5''$, 1mTorr, $KT_e = 3\text{eV}$, 100G, uniform $n = 6 \times 10^{12} \text{ cm}^{-3}$

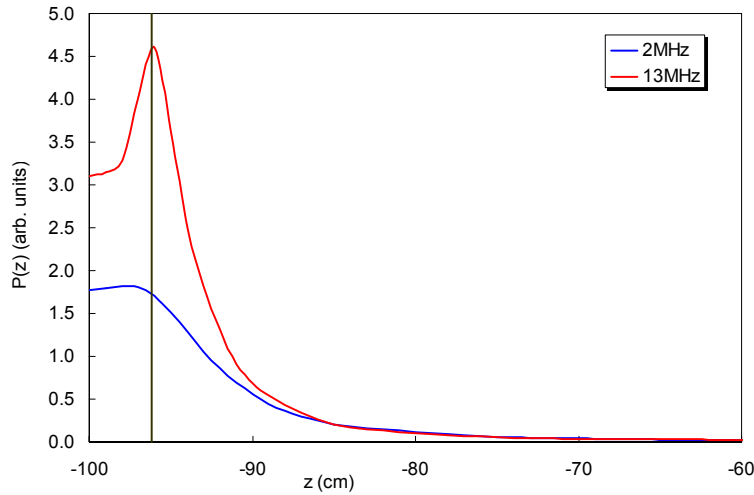


Fig. 17. Power deposition vs. z for the same conditions as in Fig. 16.

helicon is not the primary wave causing the rf absorption. As proposed by Shamrai⁹ and verified by Arnush², the helicon mode-couples to a Trivelpiece-Gould (T-G) wave at the boundary, and the latter is a slow, electrostatic wave which is rapidly damped. If we look at the radial profiles of $|\mathbf{B}|$, $|\mathbf{E}|$, and P_{in} (Fig. 18), we see that the power is deposited near the boundary by the T-G wave there, as shown by its much stronger E-field. Thus, 13 MHz is a much better frequency because of its larger and wider T-G absorption peak.

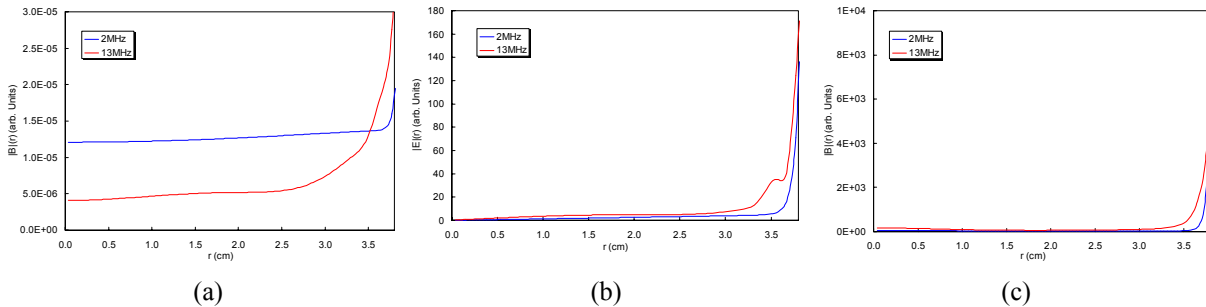


Fig. 18. Radial profiles of (a) $|\mathbf{B}|$, (b) $|\mathbf{E}|$, and (c) P_{in} for the same conditions as in Fig. 16.

5. Variation with pressure

Figure 19 shows the variation of R_p with neutral pressure. Up to 10 mTorr the difference is minimal.

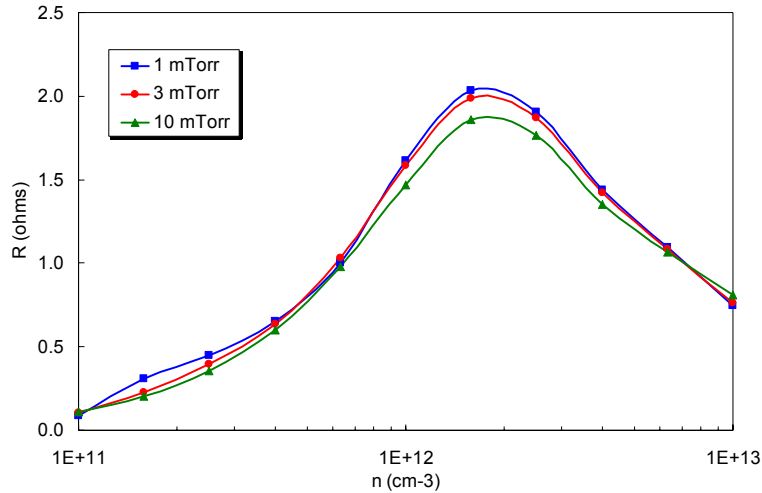


Fig. 19. Loading curves at three pressures for a 2" diam tube at 100G, 13.56MHz, and $H = 1.5"$.

6. Variation with endplate material

The optimum antenna position H depends on whether or not the phase of the wave is reversed at the end boundary. Figure 20 compares a conducting endplate with an insulating one.

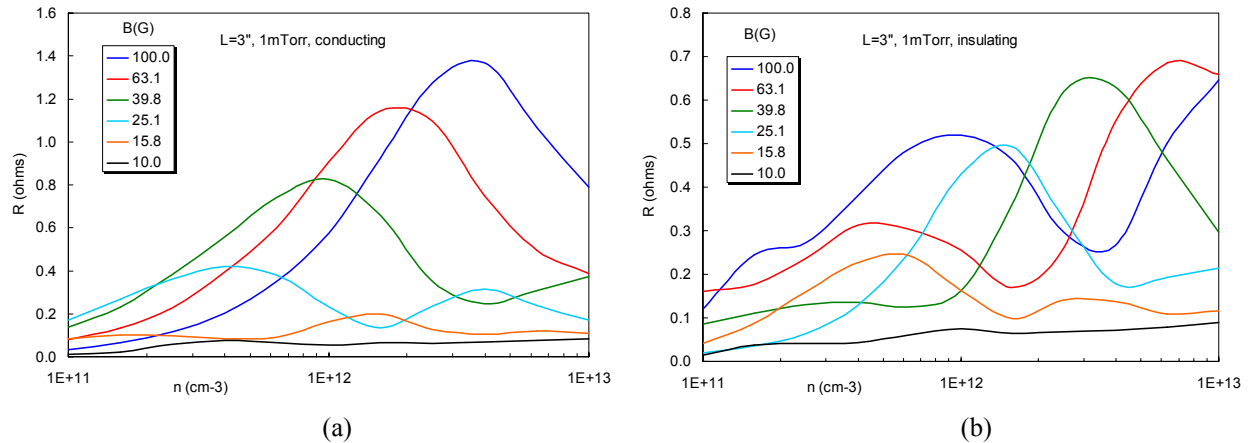


Fig. 20. Loading curves for a 2" diam tube with $H = 1.5"$ at various B-fields for (a) conducting and (b) insulating endplates.

It is clear that in this case the conducting endplate gives much higher plasma loading than the insulating one at the low-field peak.

7. Variation with antenna type

The highest densities in helicon discharges have been obtained with $m = 1$ antennas, where m is the azimuthal mode number. The two common types are the Nagoya Type III (N3) antenna, which emits waves in both the $+z$ and $-z$ directions, and the half-wavelength helical (HH) antenna, which is unidirectional. These antennas need to be about half a wavelength long, so they would not fit on short tubes suitable for use with permanent magnets. Nonetheless, we have computed R_p for both N3 and HH antennas, and it is always much smaller than for simple loop ($m = 0$) antennas for the tube sizes, B-fields, and densities being considered here. Figure 21 shows the power deposition in a 2" diam tube with a 10-cm long HH antenna as the distance H

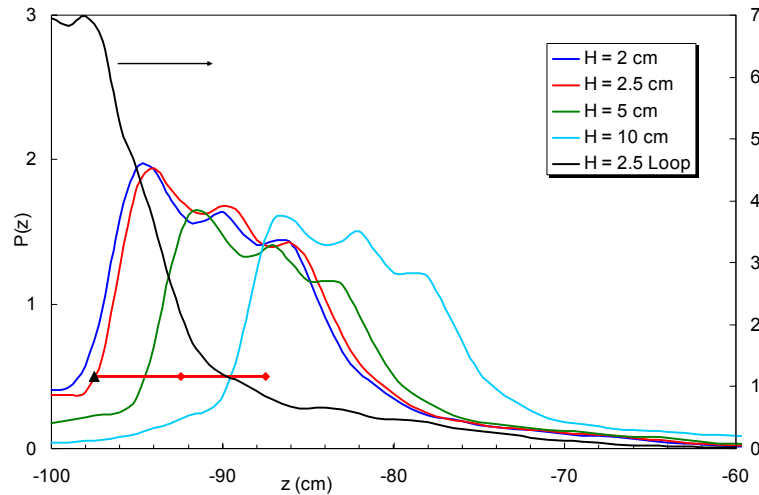
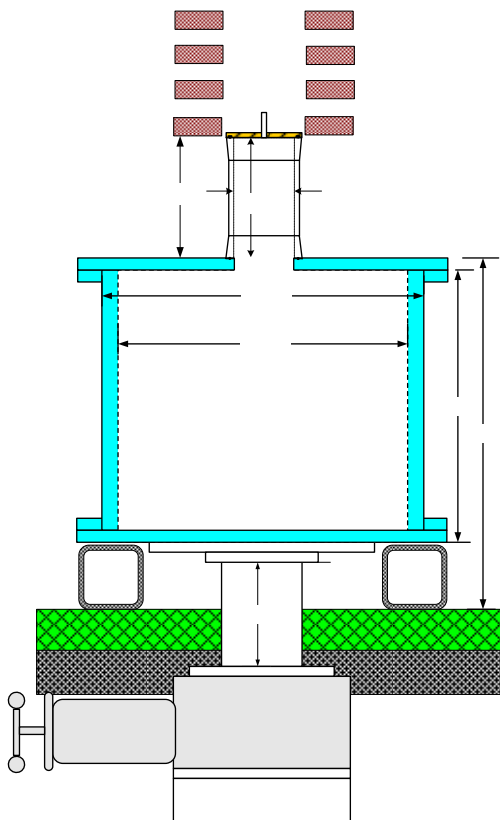


Fig. 21. Power deposition as a function of z for a 10-cm long HH antenna at various distances from the conducting endplate at the left. The red horizontal line is the position of the antenna when $H = 2.5$ cm. The corresponding deposition profile is the red curve. A loop antenna at $H = 2.5$ cm (black triangle) gives the black curve (right-hand scale). Conditions are: $KT_e = 3\text{eV}$, $p = 1\text{mTorr}$, $n = 6 \times 10^{12}\text{ cm}^{-3}$ uniform, 13.56 MHz, 100G.

between the endplate and the near end-ring of the antenna is varied. The curves do not change much in shape or amplitude and simply move with the antenna. The average loading is $R_p \approx 0.49\Omega$. By comparison, the black curve shows $P(z)$ for a simple loop antenna at $H = 2.5$ cm. Its deposition is much higher and is shown on the right-hand scale, and it has $R_p = 1.1\Omega$. Hence, there is no advantage to $m = 1$ antennas in short tubes.

C. Experimental data



The apparatus is shown in Fig. 22. The initial tests were made with the 3-inch ID tube shown, and the possibility of operation in the remote field of a stack of permanent magnets (PMs) was verified by varying the distance D between the bottom of the magnets and the top of the vacuum chamber cover. The field strength in the discharge decreases with increasing D ; the values will be given in the next section. Radial density profiles are made with two probes: $Z1$ at 7 cm, and $Z2$ at 17 cm, below the top plate. These are shown in Fig. 23.

At $D = 1\text{cm}$, the discharge is inside the magnets, and the density downstream is very low, as expected, since the field lines carry the plasma into the top flange. As D increases, n increases, in spite of the fact that the B-field is getting weaker. This is not unexpected from Fig. 11. That shows that high fields have better loading, but not at low densities. The main point is that the densities obtained are in the 10^{10} cm^{-3} , well below those desired.

Fig. 22. Diagram of test apparatus.

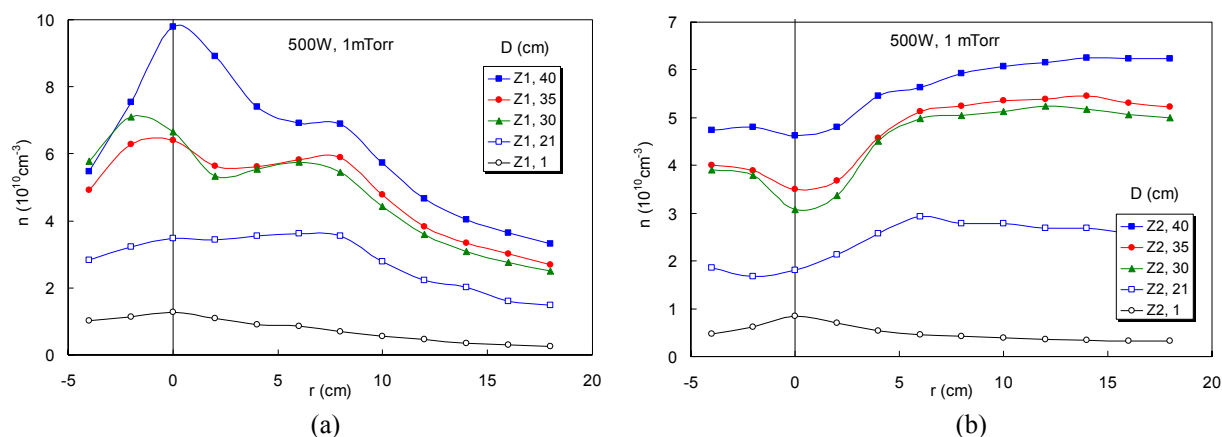


Fig. 23. Radial density profiles at (a) 7cm and (b) 17cm below the source, taken at 2 MHz, 1 mTorr, and 500W of rf at various distances D between the main chamber and the bottom of a stack of four spaced permanent magnets..

Figure 23a shows that $n(r)$ at Z1 near the source still retains the peaked profile inside the source, while Fig. 23b shows that at Z2, 10 cm further downstream, $n(r)$ has been spread out by collisional diffusion and the divergence of the field lines. The effect of pressure is shown in Fig. 24. As expected from Fig. 19, there is not much change with pressure, but the smoothing effect of collisions is evident.

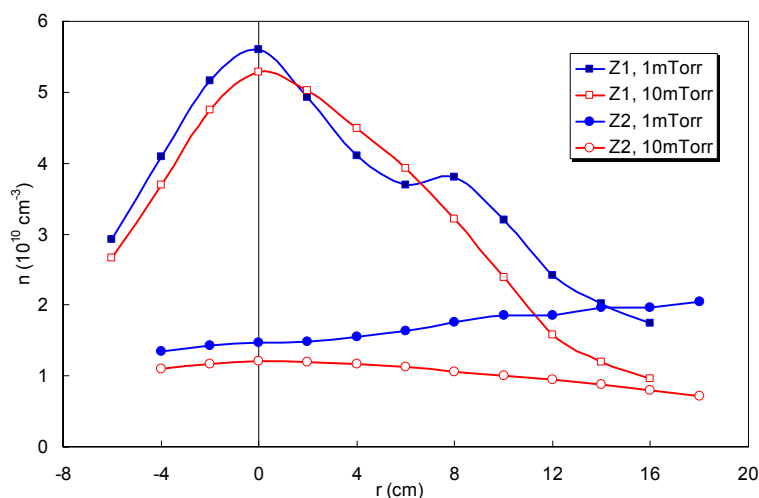


Fig. 24. Density profiles at 1 and 10 mTorr pressure with probes Z1 and Z2 and magnets at $D = 40.5$ cm.

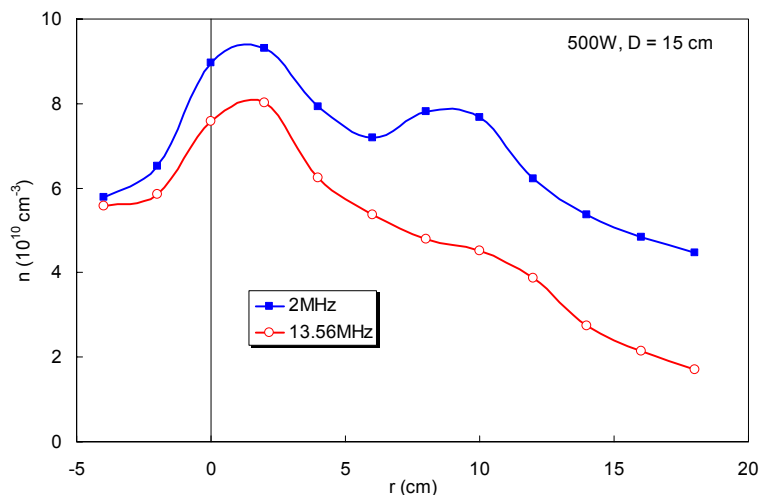


Fig. 25. Density profiles at 2 and 13.56 MHz in the 3-in. diam tube.

Comparison of frequencies is shown in Fig. 25 for the 3" diam tube. Although Fig. 15 predicts much higher loading at 13MHz, we see that the density is actually higher at 2MHz. The discrepancy is attributed to antenna coupling problems. At 13MHz, the matching circuit had to be modified, and the antenna had to have as low an inductance as possible. Thus, the antenna was a single turn carrying large current, and the circuit losses were larger. Fortunately, this problem is solved by using a smaller diameter tube, whose antenna has lower inductance.

The effect of tube diameter was checked with a 6-inch diam tube. The results are shown in Fig. 26. Although Fig. 12 shows increasing R_p with larger tubes, the downstream density with the 6" tube was disappointingly low. There are three reasons for this. The plasma resistance R_p does not take into account the amount of power required to ionize the larger volume, and the power was limited. Second, the antenna inductance is a bigger problem with the larger diameter. Third, the antenna was located at the midplane of the tube, which was longer than that of the 3" tube, and hence farther from the main chamber. Thus, the very large R_p 's with large tube cannot be used effectively.

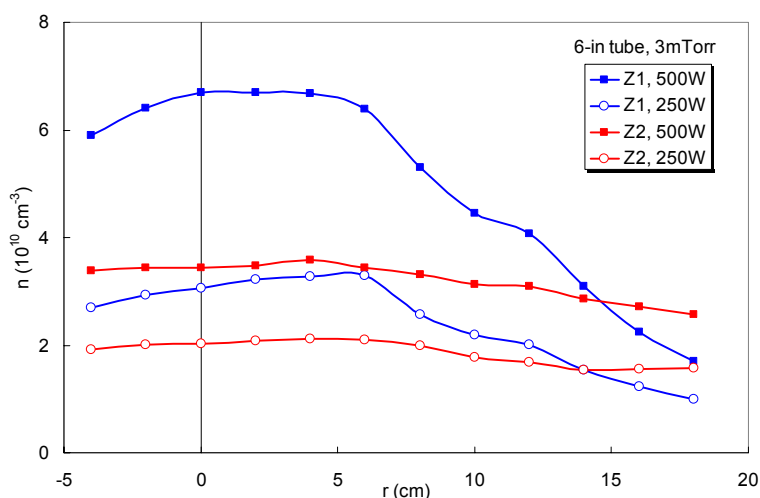


Fig. 26. Density profiles in a 6-inch diam tube at two probe positions and two rf powers.

Finally, we tried the 2" diam ("stubby") tube used in Ref. 1, shown in Fig. 27. The density on axis vs. P_{rf} is shown in Fig. 28 for different magnet positions D . We see that densities in the 10^{12} cm^{-3} range are obtained, an order of magnitude higher than possible with any of the other

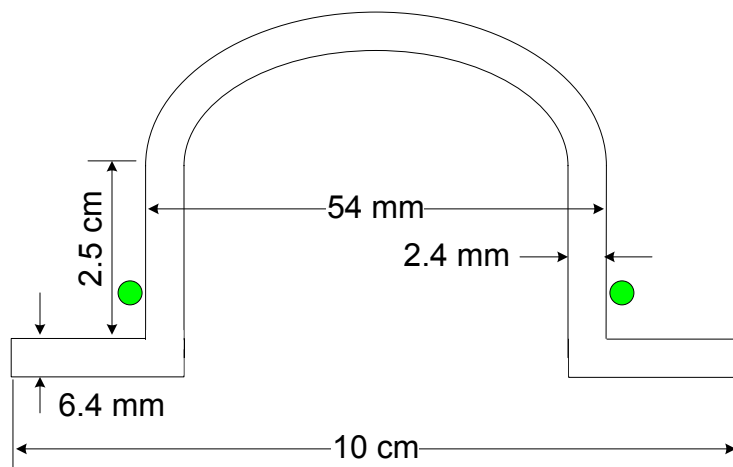


Fig. 27. The short, 2-in. diam tube used in Ref. 1.

configurations tried. In addition, the various positions D for the magnets show that the result is not sensitive to the exact value of the magnetic field. This tube configuration has a fortuitous combination of several effects. First, the tube length is optimal for the low-field peak in the 10^{12} cm^{-3} density range. Second, the smaller diameter makes a multi-turn $m = 0$ antenna possible, and the number of turns can be adjusted for the best coupling. Third, the small volume requires less rf power to fill with high density. Finally, the insulating “skirt” moves the metal flange away from the antenna, so that the antenna can be placed near the exit aperture without inducing image currents in the flange. The design of Fig. 1 is based on these considerations and should be even better than that of Fig. 27 because Fig. 20 showed that a conducting endplate is superior.

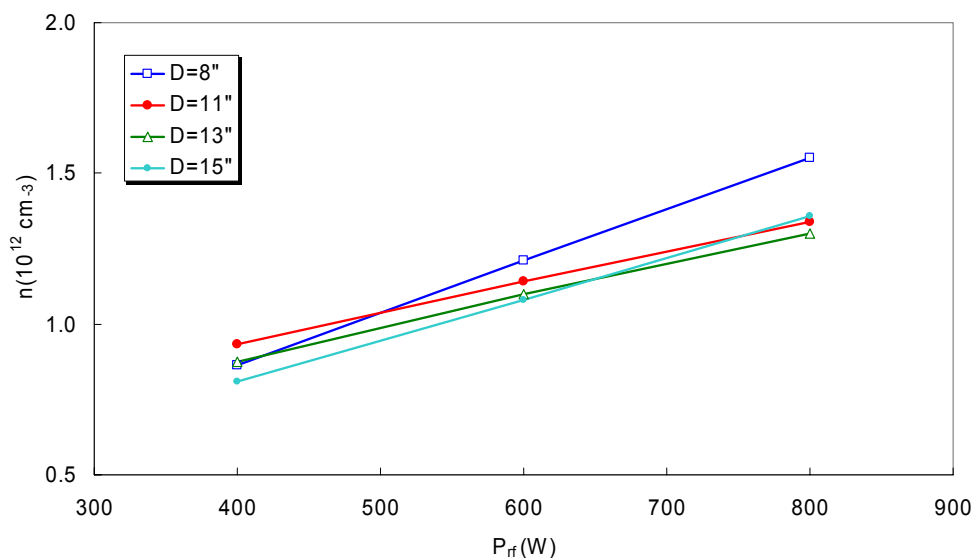


Fig. 28. Density on axis vs. P_{rf} at 13.56 MHz and $p = 18$ mTorr for the stubby tube and various magnet positions D .

Radial density profiles for the stubby tube are shown in Figs. 29 and 30.

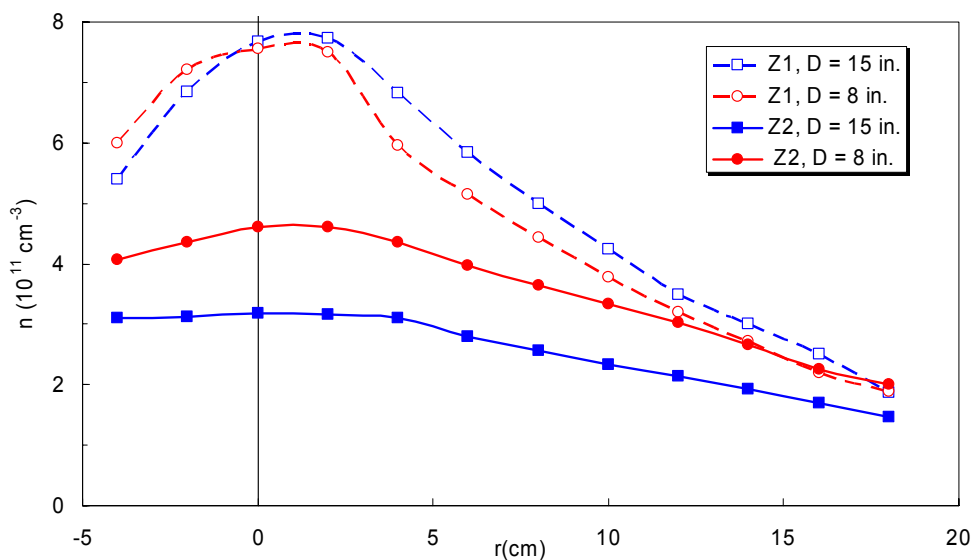


Fig. 29. Density profiles for the stubby tube at 13.56 MHz, 500W, and 10 mTorr for two magnet heights D and two probe positions $Z1 = 7.4$ and $Z2 = 17.6$ cm below the tube.

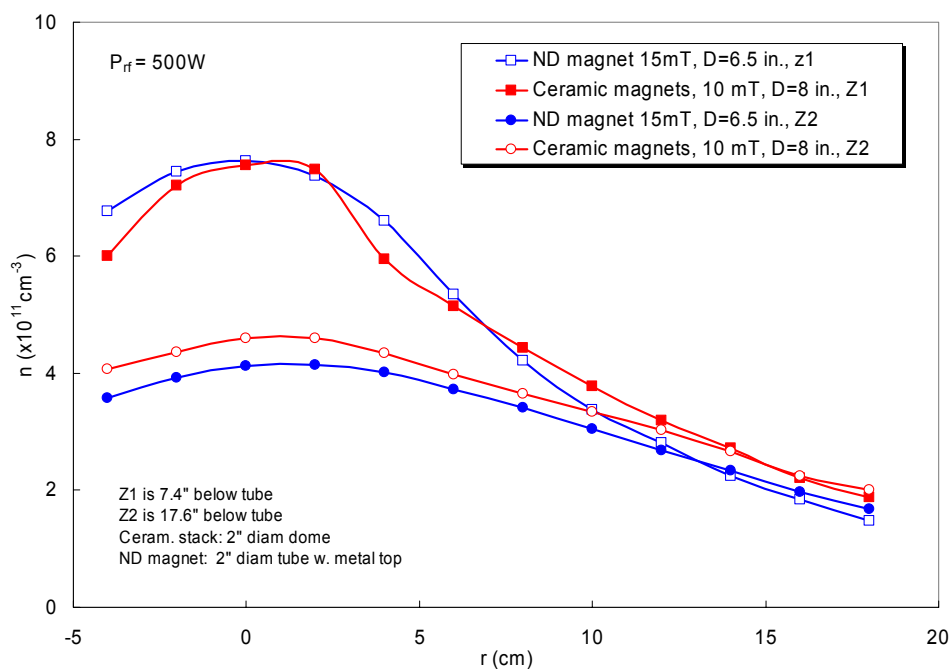


Fig. 29a. Here the $D = 8''$ curves of Fig. 29 are compared with later profiles taken with the neodymium magnet and the discharge tube of the final design. The profiles are similar, so that the calculations of uniformity for an array are valid for both configurations.

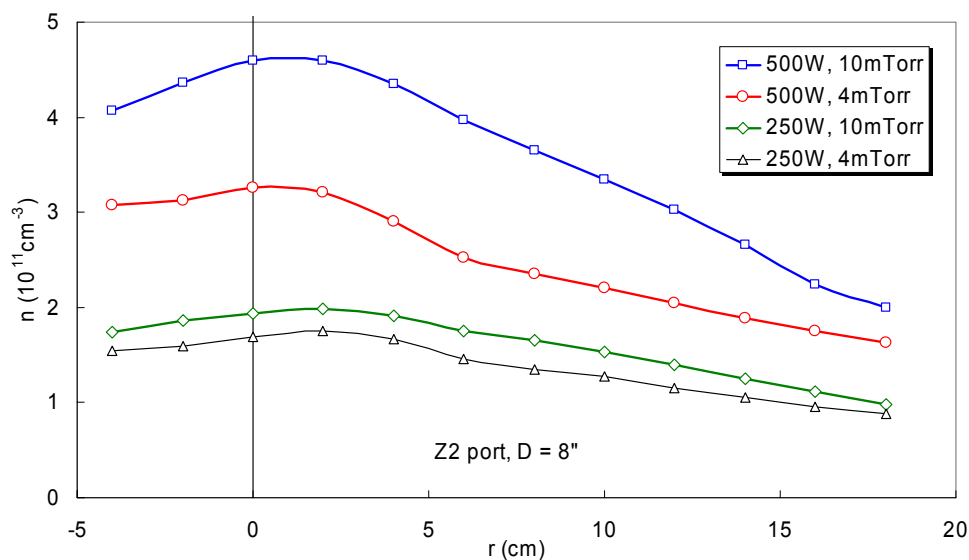


Fig. 30. Density profiles at the lower probe position for the stubby tube at 13.56 MHz, 500W, and $D = 8''$ for two pressures and two rf powers.

At 17.7 cm below the source, the density profiles are smooth, peaking just under $5 \times 10^{11} \text{ cm}^{-3}$ at 500W and 10 mTorr. These profiles are used to calculate the spacing of an array of such tubes to give a uniform distribution. With an array and with a conducting endplate, as in Fig. 1, we expect that 10^{12} cm^{-3} density will be achieved in argon at 500W per tube.

IV. DESIGN OF THE MAGNETIC FIELD

The annular magnets used for the tests described above were ceramic magnets with a permeability of 1880, with ID = 4.4", OD = 8.6", and thickness 7/8". The B-field was polarized perpendicular to the plane of the rings. In the standard configuration, the magnets were spaced 3/4" apart. The field lines Fig. 31 show clearly the stagnation point dividing the interior from the

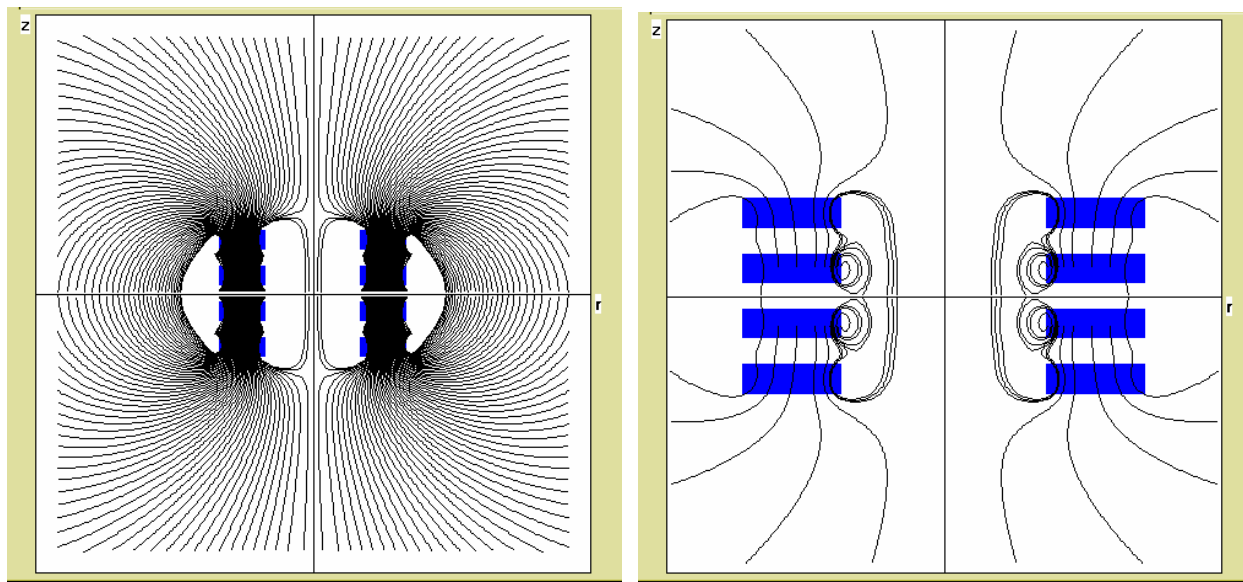


Fig. 31. Field lines on two scales for the standard PM configuration.

exterior field. The interior field strength is plotted in Fig. 32. On axis, the field is fairly uniform and reaches $\approx 300\text{G}$. At larger radii, the field is rippled by the gaps between the magnets. Note

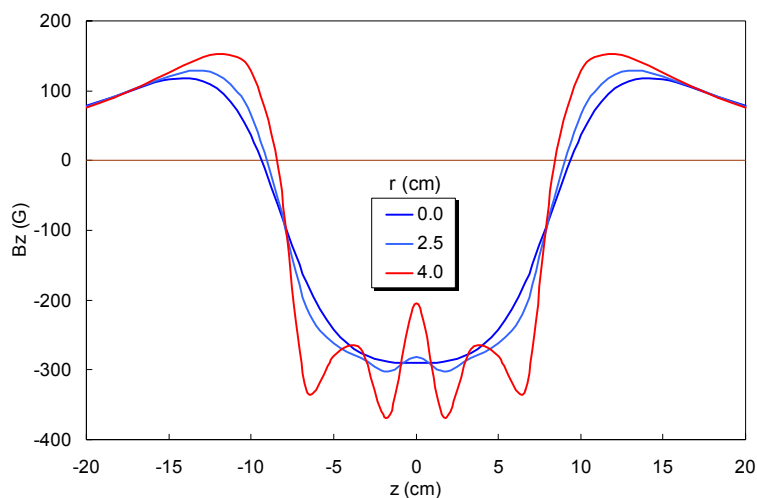


Fig. 32. Interior B-field of standard PM configuration at three radii.

that the exterior field ($B_z > 0$), however, is almost uniform in radius; it is shown in Fig. 33. Also shown are the positions of the 3-in. diam tube at various distances D used in the measurements. The B-field varies considerably along the length of a 6" tube but would be fairly uniform inside a 2" long tube.

Figure 34 shows the agreement between the calculated curve of $|B_z|(z)$ on axis with the measurements made with a gaussmeter. This yielded the absolute value of the permeability μ . We next studied the effect of changing the magnet dimensions.

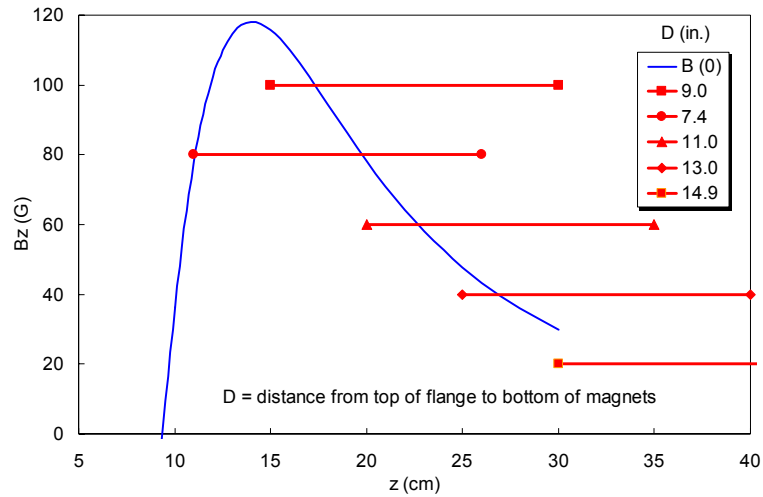


Fig. 33. Exterior B-field of the standard PM configuration. The horizontal lines are positions where the 3" diam, 6" long tube is placed for measurements at various magnetic fields.

Figure 35 shows the effect of varying the ID while keeping the width $w = (OD-ID)/2$ constant. The interior field on axis is rippled as the ID is made smaller, but the exterior field is nearly unchanged, with a small increase of $|B_z|$ as the ID is increased.

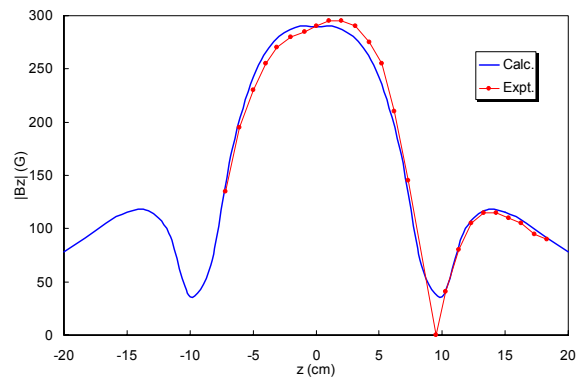


Fig. 34. Calibration of calculated $|B_z|(z)$ against gaussmeter measurements.

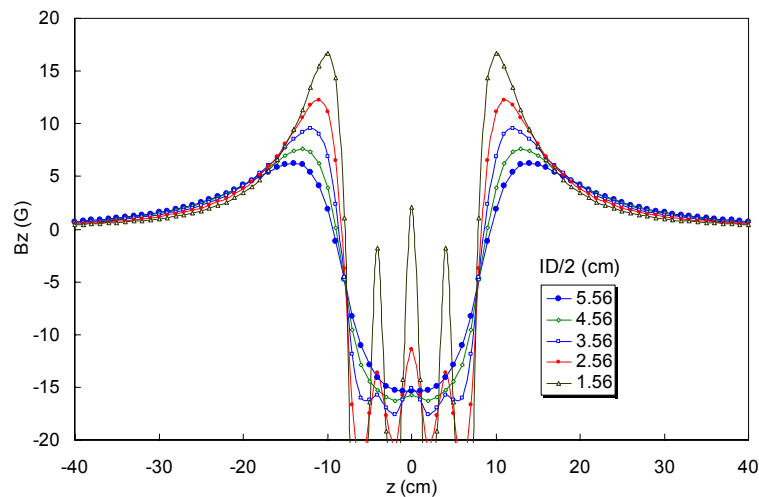


Fig. 35. Variation of calculated $|B_z|(z)$ for various magnet IDs in a spaced stack of four rings. The values are for $\mu = 100$.

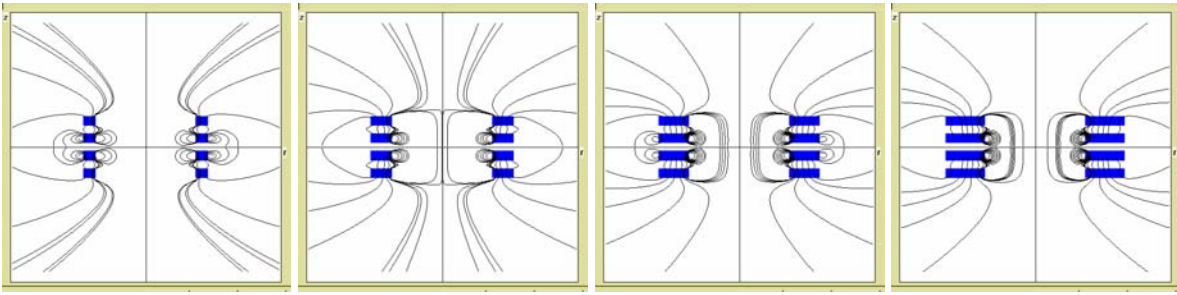


Fig. 36. PM configurations with constant ID and various widths.

If w is changed keeping the ID constant, the configuration changes as shown in Fig. 36. Both the interior and exterior fields increase with OD, as seen in Fig. 37. However, the increase is slower than linear with OD, as shown in Fig. 38.

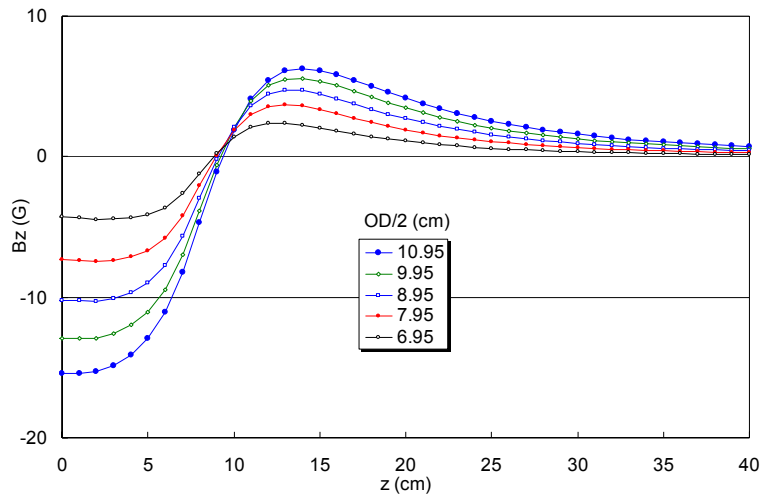


Fig. 37. B_z vs. z for PMs with different ODs but the same ID. The values are for $\mu = 100$.

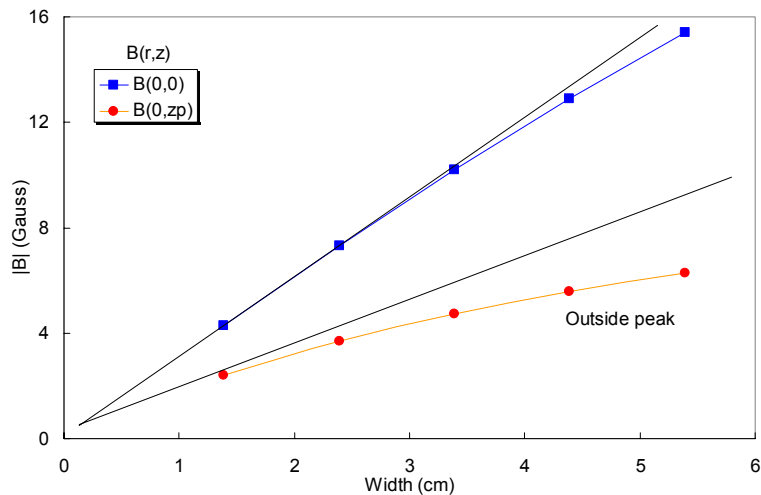


Fig. 38. B_z vs. z for PMs with different ODs but the same ID. The top curve is for the field at the center of the magnet stack. The lower curve is for the exterior field at its peak. The values are for $\mu = 100$.

The spacing between magnets in a stack can also be changed, as shown in Fig. 39. Reducing the spacing increases the field slightly, as shown in Fig. 40a. However, the field gradient is not changed if the stack is moved vertically so that the field strength is the same. This is shown in Fig. 40b.

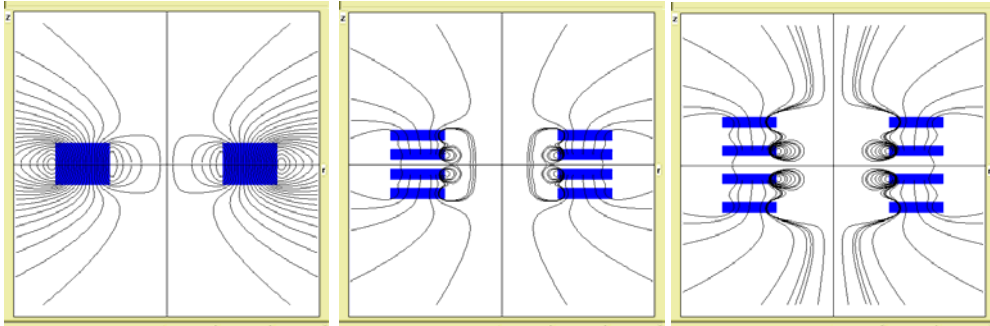


Fig. 39. Field configurations with different spaces between magnets.

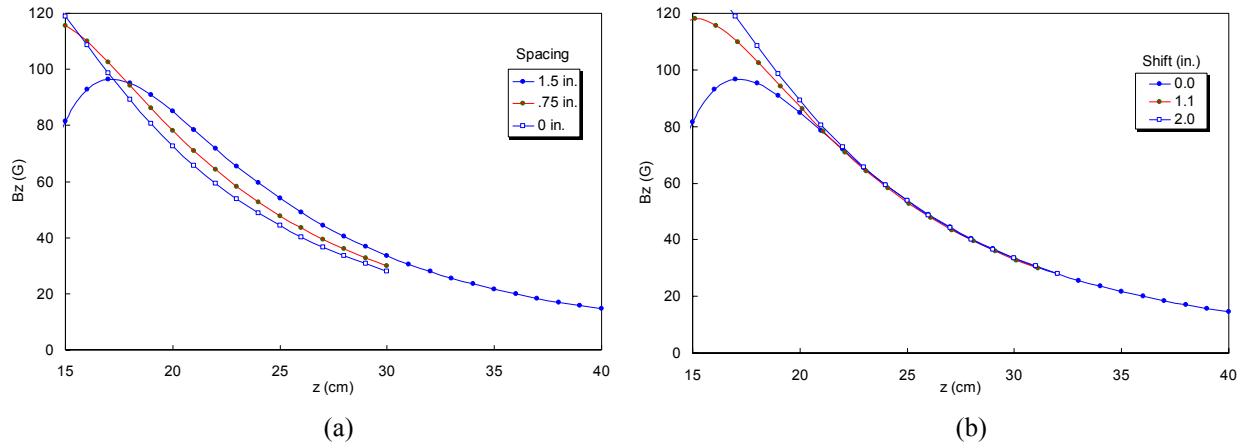


Fig. 40. (a) B_z vs. z for the exterior field with varying spacing between magnets. (b) The same curves as in (a) but shifted horizontally on the graph (vertically in the experiment). The values are for $\mu = 1880$.

From these trials we conclude that a) spacing of magnet rings has no advantage, b) the B-field magnitude can be increased by increasing the number of stacked rings or the OD of the rings, or by choosing a ferromagnetic material with higher μ , and that the ID of the rings can be decreased to match smaller discharge diameters. The design of Sec. I was based on these studies.

V. CALCULATIONS FOR THE FINAL DESIGN

From the calculations of Sec. III, we decided on the discharge tube of Fig. 1. To fit this tube, PMs of 3" ID, 4" or 5" OD, and $\frac{3}{4}$ " thickness were considered; their field shapes are shown in Fig. 41. The configuration of Fig. 41d was chosen as the most compact one with strong field. The field strength and uniformity inside the discharge tube is shown in Fig. 42. If the ≈ 5 cm-long tube is located between $D = 6$ and 11 cm, the field is above 100G everywhere inside it if $\mu = 1880$. Note that the tube spans the plane of highest external field, as shown in Fig. 2 and in Fig. 43b below. Computations like Fig. 42 were made for the configurations of Fig. 41 and several others.

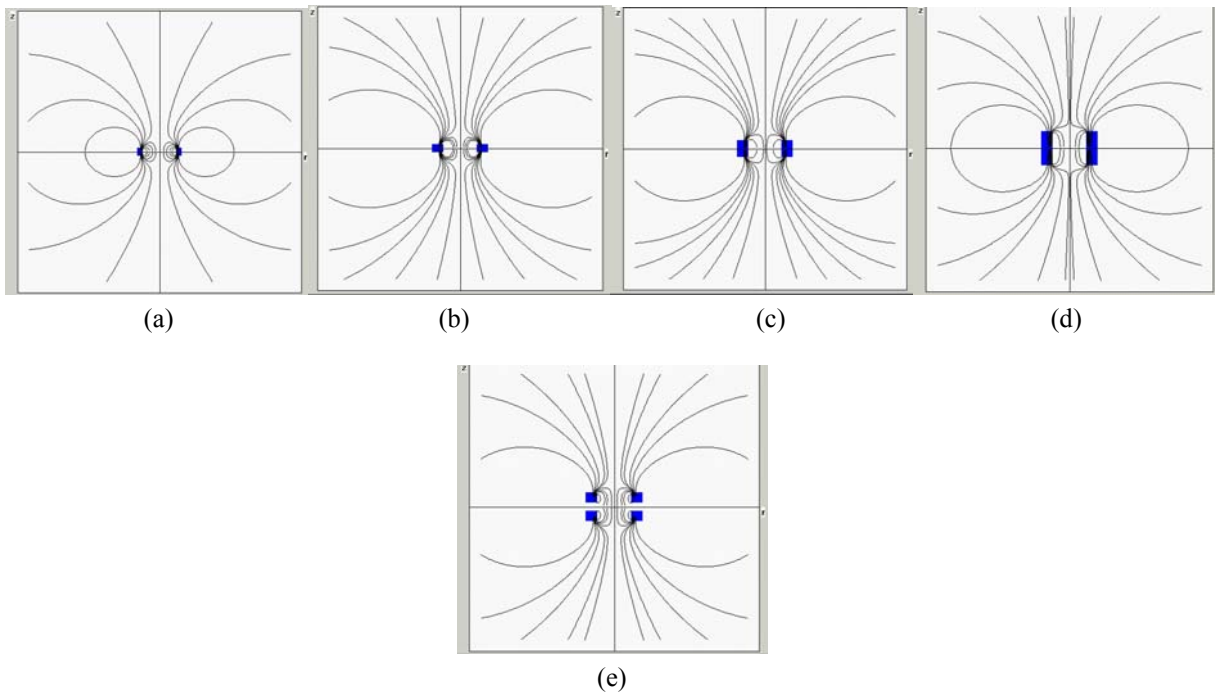


Fig. 41. Field plots for (a) one 3×4, (b) one 3×5, (c) two 3×5, (d) four 3×5, and (e) two 3×5×7/8 (spaced) magnets.

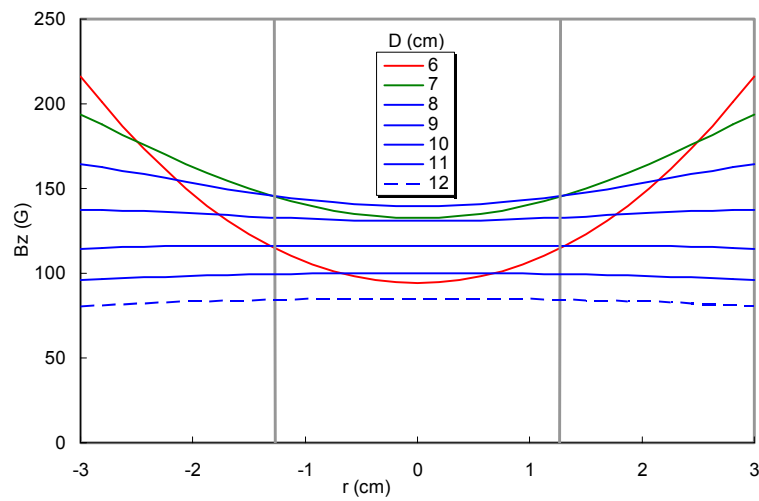
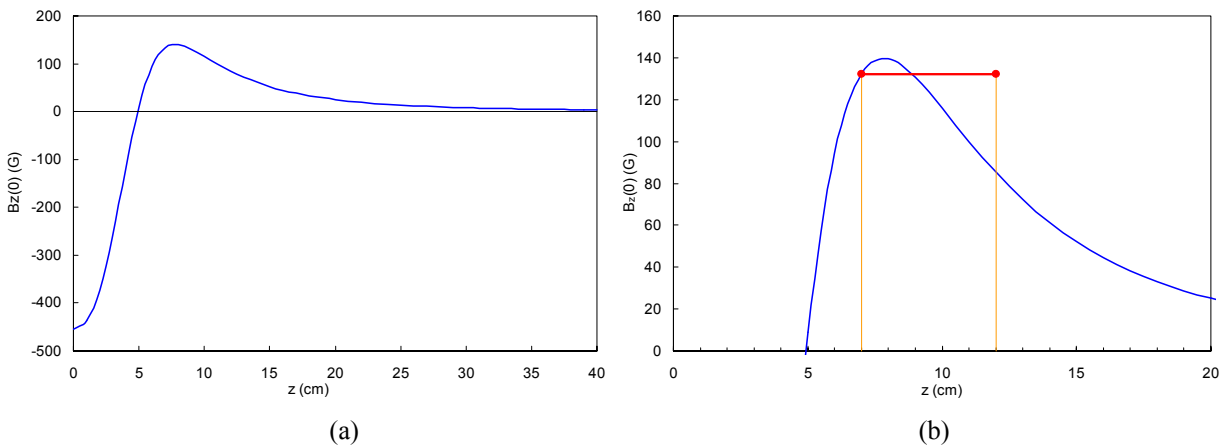


Fig. 42. B_z vs. r at various distances D below the magnet stack of Fig. 39d. The vertical lines mark the diameter of the tube. The $D = 6$ and 7 cm lines are in the converging part of the external field.



(a)

(b)

Fig. 43. Field strength of four $3 \times 5 \times 3/4$ " unspaced magnets on axis (a) everywhere and (b) in the external region. The position of the discharge tube is marked. The coordinate z is measured from the midplane of the stack.

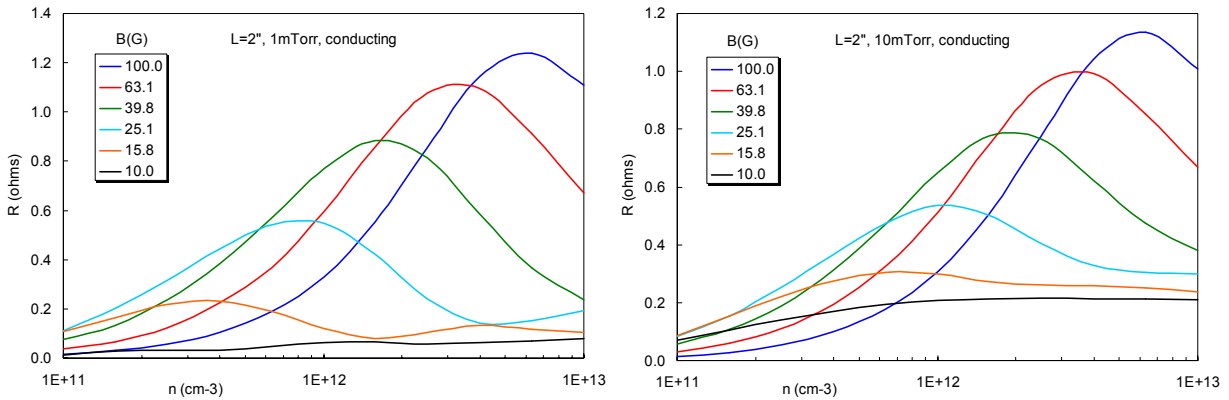


Fig. 44. R_p vs. n and B for a stubby tube with an $m = 0$ antenna near the bottom, for Ar pressures of 1 and 10 mTorr.

HELIC calculations for the plasma resistance near the low-field peak for $p = 1$ and 10 mTorr are shown in Fig. 44. We see that, with a conducting endplate, B-fields ≥ 100 G will give plasma loading $\geq 1 \Omega$ for interior densities in the high 10^{12} cm^{-3} range. With adjustment of the height D , strong magnets can give fields from 60 to 150 G to provide the best loading for the designed tube size.

The magnets used for testing are ceramic magnets, which, together with Neodymium Iron Boron magnets are the least expensive. Samarium Cobalt and Alnico magnets are much more expensive. The difference between NdFeB and ceramic is that NdFeB has about three times the field strength and has to be formed in sectors to make a ring, while ceramic can be cast into a ring in a single piece. However, the setup charge for ceramic magnets of the required size is large, and NdFeB turns out to be cheaper for an experimental device. When costs and convenience are considered, NdFeB is the preferred material. We therefore settled on NdFeB magnets of 3" ID, 5" OD, and 1" thickness. Inside the magnets, the remnant magnetic field of Ne35 material should be 12.3 kG. The computed field lines are shown in Fig. 45. The radial B_z field profiles at various distances below the magnet are shown in Fig. 46. The dashed rectangles show

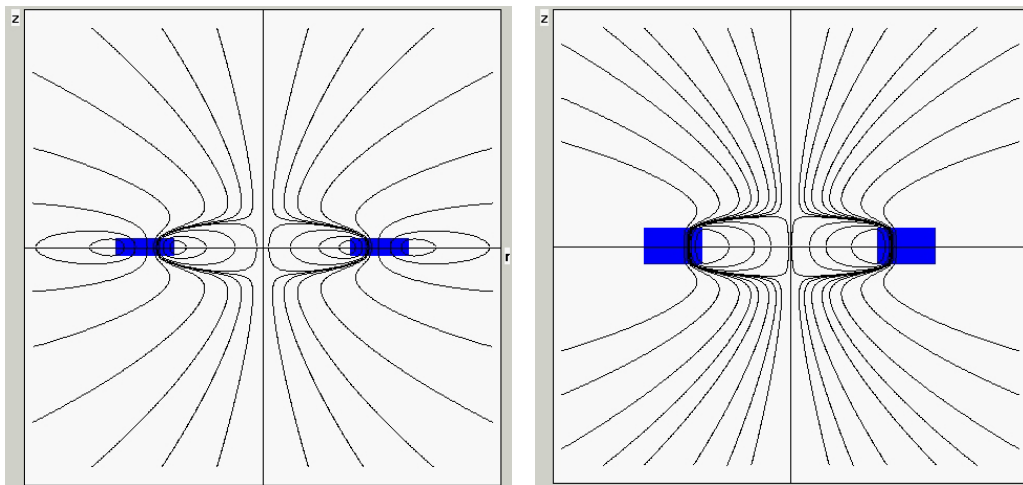


Fig. 45. Field lines of (left) a single PM and (right) two PMs with ID = 3". OD = 5", and thickness 1".

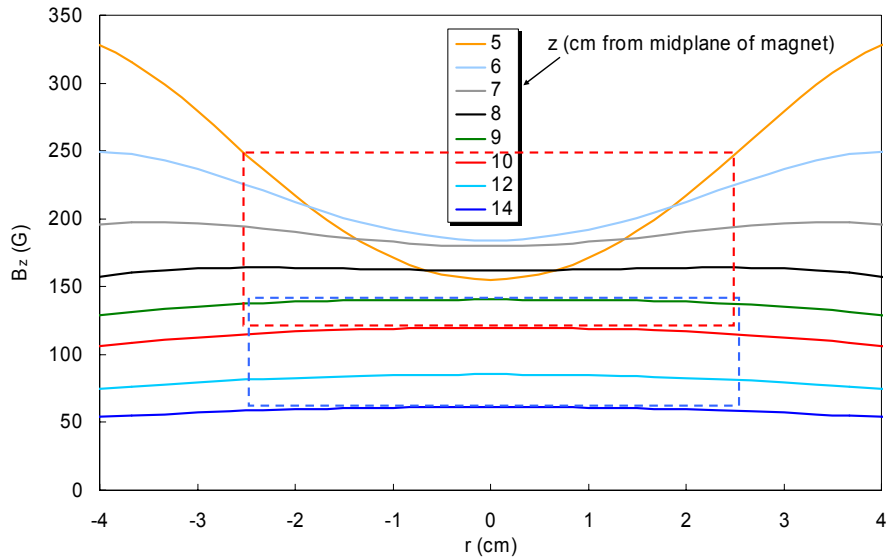


Fig. 46. $B_z(r)$ at various distances z below the midplane of the PM in Fig. 45.

possible positions of a 2" diam, 2" long discharge tube. The lower position has a very uniform field varying from 125 to 50G. The upper position has more radial nonuniformity, but the field is higher than 100G everywhere, going as high as 250G.

VI. DESIGN OF THE ARRAY

To determine the optimum spacing between tubes to obtain a uniform density at the substrate, we first fitted the radial profile of the top curve in Fig. 30 with an analytic expression. This curve is for the stubby tube of Fig. 27 and four stacked and spaced ceramic magnets located at $D = 8$ in. above the bottom of the tube. It is for 500W at 13.56MHz and 10 mTorr of argon and at a distance $Z_2 = 17.7$ cm below the source. Then, we added the density from each tube of an array in which the rows were staggered. The distance L between tube centers in a row was varied, as well as the distance $2d$ between rows. The geometry is shown in Fig. 47. The density $n(z)$ is plotted for various y and $L = 25$ cm in Fig. 48. We see that the ripple is large at $y = 0$ under the tubes but is much smaller at $y = 10$ cm. Variation of ripple vs. L is given in Fig. 49.

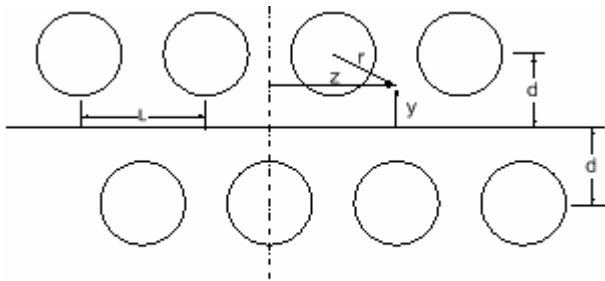


Fig. 47. Geometry for array calculations.

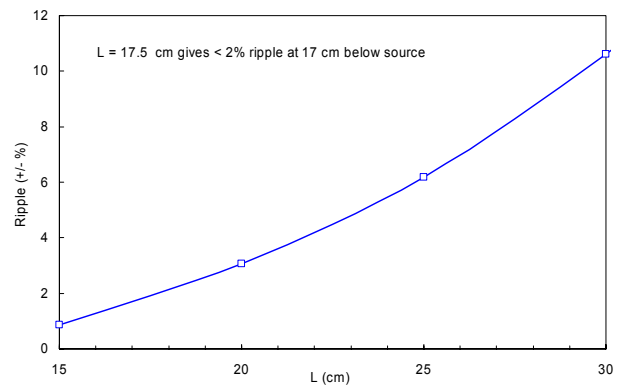


Fig. 49. Density ripple vs. L .

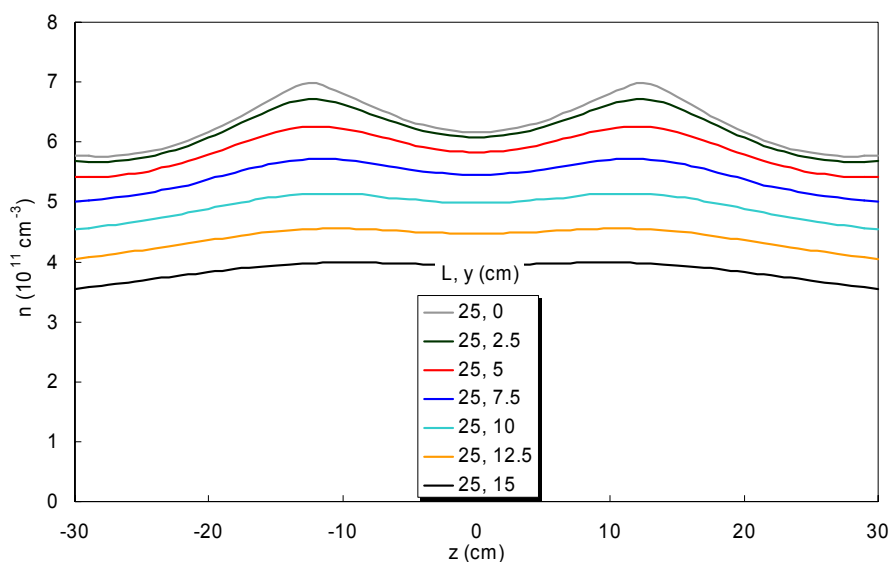


Fig. 48. Computed density profiles $n(z)$ at various distances y from a single row of tubes L cm apart.

We see that $\pm 2\%$ ripple can be obtained for $L = 17.5$ cm at 17.7 cm below the tubes.

This degree of uniformity would be suitable for deposition of optical coatings or for processing of flexible displays, but it is not necessary for web coaters, which are one-dimensional systems and require only that the y -averaged density be uniform. Figure 50 shows the computed density at various y for two rows of four tubes each. The thick and thin curves of the same color are the same y value relative to each row. These are 180° out of phase because the rows are staggered. The dotted line shows the average density to which the substrate is exposed as it passes under the two rows of sources. (The value of $\langle n(y) \rangle$ depends on the range of y averaged, but it is proportional to the ion flux impinging on the substrate.) This average is extremely uniform for $L = 30$ cm, and L can easily be increased for this application at the expense of density.

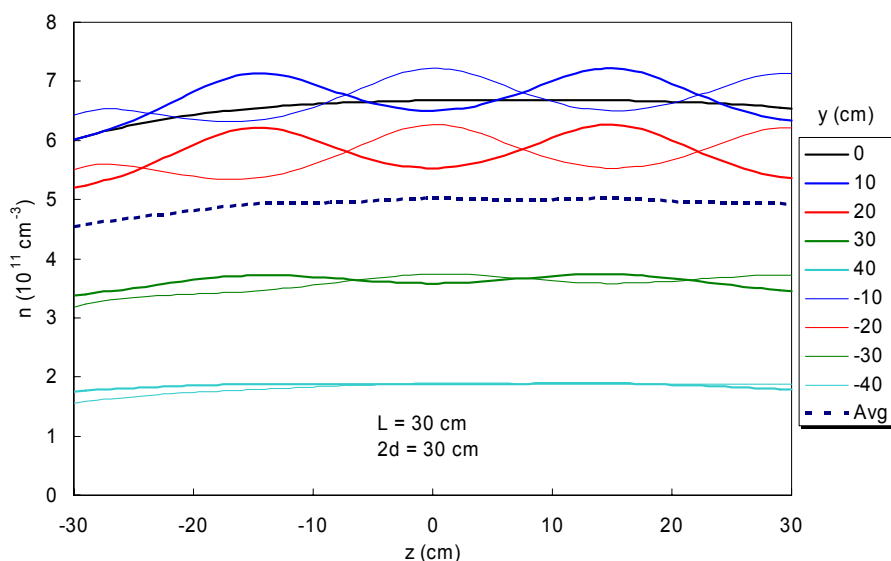


Fig. 50. Density $n(y,z)$ and $\langle n(y) \rangle$ (---) for two staggered rows of sources.

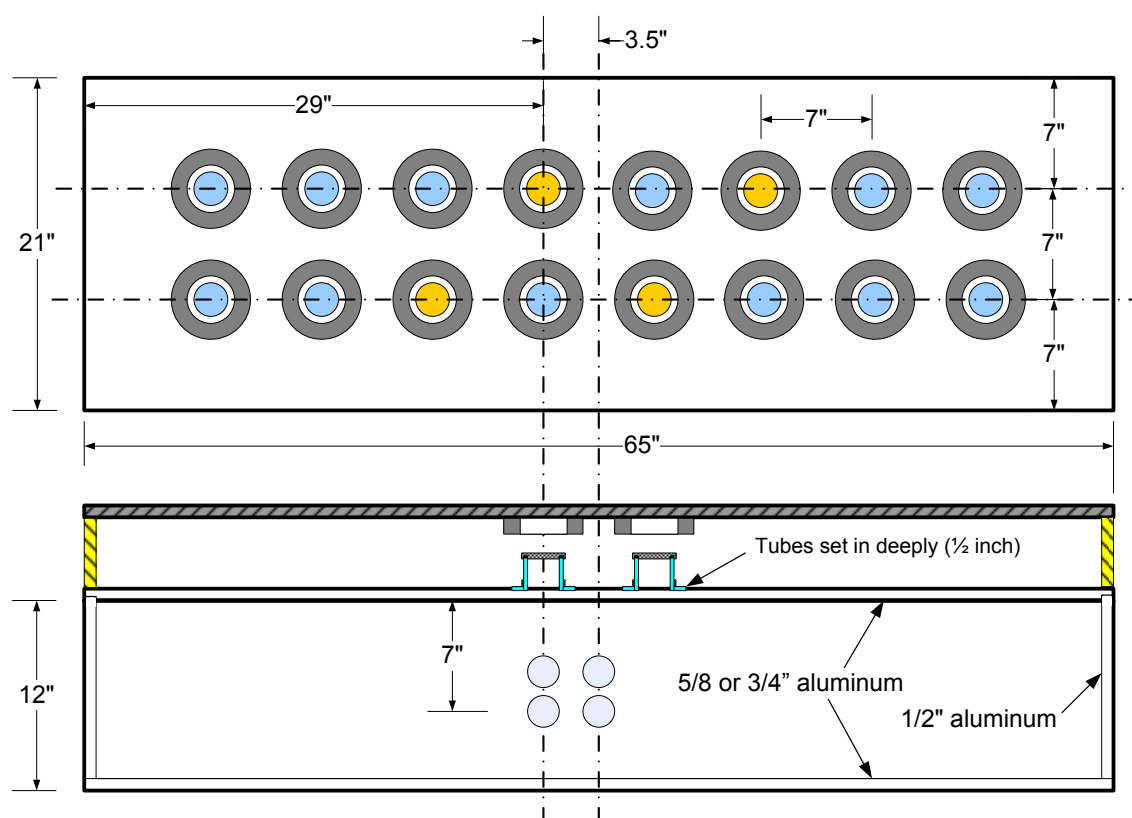
On the basis of these computations, we have designed the test chamber shown in Fig. 51. The dark annuli are the NdFeB magnets. The small circles are the 2" diam plasma tubes. The blue ones are used to test the web coater application: staggered, with large L . The eight central

tubes are used to test uniformity for 2D applications. Although the magnets are not the ceramic ones assumed in the computations, there should be little difference except in cost. In any case, there are two adjustments to optimize the density and uniformity: the distance Z from the source to the substrate, and the distance D from the magnets to the top flange. The latter is adjusted by changing the four corner posts (shown in yellow) holding up the magnet plate. This plate is of magnetic iron, and the magnets hang from it without support. A third adjustment is to stack two PMs to essentially double the field for a given D . The field lines for this are shown in Fig. 45; the spacing of the lines is arbitrary and not significant.

Note that the use of a conducting endplate on each tube allows the plasma potential to be fixed if the plasma sees only insulating materials in the main chamber. A dc bias can then be applied to the substrate with an RF bias power supply.

VI. ACKNOWLEDGMENTS

This work was supported by the National Science Foundation, Grant No. DMI-0115570.



Endplates: gas feed and
probe port at each end.

Fig. 51. Layout of test chamber designed for up to eight helicon sources.

REFERENCES

- ¹ F.F. Chen, J.D. Evans, and G.R. Tynan, *Plasma Sources Sci. Technol.* **10**, 236 (2001).
- ² D. Arnush, *Phys. Plasmas* **7**, 3042 (2000).
- ³ F.F. Chen, *Phys. Plasmas* **10**, 2586 (2003).
- ⁴ K. P. Shamrai, *Plasma Sources Sci. Technol.* **7**, 499 (1998).
- ⁵ M.A. Lieberman and A. J. Lichtenberg, *Principles of Plasma Discharges and Materials Processing* (Wiley, New York, (1994), 2nd ed., p. 333.
- ⁶ F.F. Chen and J.P. Chang, *Principles of Plasma Processing* (Kluwer/Plenum, New York, 2002), p. 71.
- ⁷ V. Vahedi, *Thesis*, University of California, Berkeley (1993).
- ⁸ V.F. Virko, G.S. Kirichenko, and K.P. Shamrai, *Plasma Sources Sci. Technol.* **11**, 10 (2002).
- ⁹ K. P. Shamrai and V. B. Sharanov, *Plasma Phys. Controlled Fusion* **36**, 1719 (1994).